ADVANCED FUNCTIONAL MATERIALS
www.afm-journal.de

Substrate Stress Relaxation Regulates Cell-Mediated Assembly of Extracellular Matrix

*Jonah L. Voigt, Jens Timmer, and Elisabetta Ada Cavalcanti-Adam**

The viscoelasticity of the extracellular matrix (ECM) regulates diverse cellular functions, yet its influence in guiding ECM assembly and organization under physiologically relevant stiffness remains poorly defined. In this study, silicone-based substrates with comparable stiffness (≈80 kPa) but distinct stress relaxation profiles are used to investigate how matrix viscoelasticity affects cellular mechanosensing and cell-mediated ECM remodeling in the stiff regime. Increased substrate stress relaxation enhances fibronectin reorganization, focal adhesion maturation, and traction force generation for similar fibronectin surface density. Cells on viscoelastic substrates exhibit increased nuclear localization of YAP and form β1 integrin-enriched adhesions, correlating with localized ECM reorganization. These findings reveal that mechanical properties alone, decoupled from biochemical cues, are sufficient to direct ECM reorganization. This platform allows dissecting mechano-regulated tissue remodeling and designing mechanically tunable biomaterials for regenerative medicine.

1. Introduction

In tissues, the mechanical properties of the extracellular matrix (ECM) are known to regulate cell behavior, including proliferation, migration, and differentiation, among others.[1–4] While the role of ECM stiffness in regulating these processes has been extensively studied, emerging evidence highlights the importance of ECM viscoelasticity, specifically time-dependent stress relaxation, as a key regulator of cell behavior. Using materials that mimic viscous ECM features, it has been shown that stress relaxation alone can influence cell spreading, migration, and even stem cell fate.[5–8] Furthermore, enhanced matrix viscoelasticity, independently of stiffness, has also been found to promote cancer cell progression in vivo.[9]

Biological tissues exhibit a wide range of elastic and viscoelastic properties spanning several orders of magnitude, and this mechanical diversity plays a central role in regulating cell functions involved in tissue development, repair, and disease.[10–12] Soft tissues such as brain and adipose tissue exhibit low elastic moduli in the range of 0.1 to 1 kPa, whereas stiffer tissues like muscle, cartilage, and cortical bone display moduli extending up to the range of GPa.[10,13,14] Likewise, viscoelastic parameters – such as stress relaxation time and creep compliance – also vary considerably between tissues, reflecting their functional demands.[8] This mechanical diversity is crucial in guiding cellular processes, including ECM deposition and remodeling. However, the interplay between stiffness and viscoelasticity is difficult to dissect for in vitro systems, making it challenging to isolate their respective contributions in controlling cell behavior.

To address this, extensive efforts have focused on developing ECM-mimetic materials that offer precise control over matrix mechanics, enabling mechanistic studies of how individual physical cues regulate cell function at both single-cell and tissue scales.[15–18] Beyond regulating cell adhesion and fate, matrix mechanics, particularly viscoelastic stress relaxation, is also increasingly recognized as a critical determinant of ECM assembly and, consequently, tissue morphogenesis and function. Mechanical cues guide the organization of fibrillar ECM scaffolds, which are indispensable for tissue structural integrity and to direct cellular behavior during repair and disease progression.[1,12] Understanding how substrate mechanics alone orchestrate ECM fibrillogenesis is of broad relevance for regenerative medicine and tissue engineering, where designing bioinspired materials that recapitulate not only biochemical but also mechanical cues is a key challenge. In this context, functional materials with tunable viscoelastic properties provide an essential tool for both basic mechanobiology and applied biomaterials research.[5,19–21] However, most existing studies have examined viscoelasticity in the soft regime, and fewer have explored its role under stiff mechanical conditions, which are relevant for many load-bearing tissues and disease states.[22,23]

Silicone-based elastomers, such as polydimethylsiloxane (PDMS), offer a practical alternative to hydrogels for studying mechanotransduction due to their stable mechanical properties

---

J. L. Voigt, J. Timmer, E. A. Cavalcanti-Adam
Cellular Biomechanics
University of Bayreuth
Universitätsstraße 30, 95447 Bayreuth, Germany
E-mail: eacavalcanti@uni-bayreuth.de

J. L. Voigt, E. A. Cavalcanti-Adam
Max Planck Institute for Medical Research
Jahnstraße 29, 69120 Heidelberg, Germany

J. Timmer
Department of Biosystems Science and Engineering
Eidgenössische Technische Hochschule (ETH) Zürich
4056 Basel, Switzerland

DOI: 10.1002/adfm.202509352

and straightforward ECM protein coating without chemical activation. Previously, we used such PDMS substrates (Sylgard 184) to mimic a wide range of tissue stiffnesses.[24] One major advantage of these over commonly used hydrogels, such as polyacrylamide (PAA) is the ease of ECM protein coating. No chemical cross-linkers or unstable reagents (e.g., Sulfo-SANPAH) are required; proteins adsorb directly to the substrate surface, with coating density readily tuned by adjusting protein concentration or incubation time.[24] Despite similar biochemical surface properties, we show here that mechanical differences, specifically in stress relaxation, can drive distinct cellular outcomes, including focal adhesion maturation and ECM fibrillogenesis. This highlights the primacy of mechanical over chemical cues in regulating cell-material interactions, a key consideration in functional biomaterials design.[15]

A large variety of silicone substrates exist with differing mechanical properties, including viscoelasticity. For this study, three silicone-based materials, QGel 920, Sylgard 184, and Sylgard 186, were selected to fabricate substrates of equal stiffness (≈80 kPa) but varying stress relaxation. Each consists of two components mixed in defined ratios to achieve the desired stiffness while being inherently more or less viscous, resulting in substrates with significantly different stress relaxation. They were classified as low stress relaxation (low SR), medium stress relaxation (med SR), and high stress relaxation (high SR), and subsequently, this setup enables a controlled study of how substrate stress relaxation affects cell behavior in the stiff regime.

Sylgard 184 is widely used in cell culture and microfluidic device fabrication and is well-characterized in biomedical research.[24–27] QGel 920 has gained interest due to its optical properties, as its reflective index closely matches that of glass, making it compatible with TIRF-microscopy while enabling stiffness tuning,[28] and we have found it to undergo less stress relaxation than Sylgard 184 at equivalent stiffness. Conversely, Sylgard 186 is similar to Sylgard 184 but shows significantly more stress relaxation, thus allowing us to fabricate three distinct stiff substrates that differ only in their stress relaxation behavior. While most studies on viscoelasticity have focused on soft substrates, growing interest in how stress relaxation influences cells on stiff matrices has led to models such as the “pull-and-hold” molecular clutch mechanism of mechanosensing.[29] This further highlights the need for user-friendly, tunable substrates, particularly at higher stiffness, which are relevant to many tissues. Our combination of substrates addresses this need, enabling studies on how stress relaxation influences cell function and ECM assembly in stiff environments.

The mechanical characteristics of these materials, including Young’s modulus, viscous energy dissipation, tan(δ), and water contact angle, were characterized. Surface coating with the ECM protein fibronectin (FN) was quantified over time, and its effects on surface hydrophobicity were assessed. Substrate suitability for cell culture was confirmed, and we investigated how stress relaxation modulates cell adhesion and mechanosensing, particularly via nuclear localization of yes-associated protein 1 (YAP1), a key regulator of mechanotransduction sensitive to viscoelasticity.[5,30,31] We found that substrate stress relaxation supported focal adhesion development and size. Furthermore, fibronectin fibrillogenesis occurred exclusively on viscoelastic substrates, correlating with elevated cellular traction, a prerequisite for ECM assembly.[32] These findings demonstrate that stress relaxation alone guides fibrillar matrix assembly by directing cellular mechanics in stiff environments. This work establishes a practical system to study how substrate stress relaxation at high stiffness shapes cell behavior and ECM remodeling, offering insights for the design of next-generation materials for tissue regeneration where mechanical cues are as critical as biochemical ones.

2. Results and Discussion

2.1. Stiff Substrates with Varying Stress Relaxation Mimic Extracellular Matrix Mechanical Properties

The mechanical properties of the substrates were characterized using nanoindentation, with the resulting values summarized in **Table 1**. Young’s moduli were first measured for single samples (**Figure 1A**), revealing no significant differences among QGel 920, Sylgard 184, and Sylgard 186, with only slight deviations across the substrate surfaces. All substrates exhibited average stiffness values around 80 kPa, which aligns with the mechanical properties of biological tissues such as skin, cornea, or skeletal muscle.[10] To ensure reproducibility and confirm the consistency of the fabrication process, three independent samples were measured for each material, showing minimal variability in stiffness values (Figure S1, Supporting Information). Representative loading curves for the three substrates as measured with the nanoindenter are shown in Figure S2 (Supporting Information).

To investigate material viscoelasticity, we quantified both stress relaxation and dynamic mechanical properties. Stress relaxation was recorded with a constant depth of indentation over a 60-s period, revealing marked differences between substrates based on their normalized force decay curves (Figure 1B). QGel 920 showed minimal stress relaxation, consistent with low energy dissipation and elastic behavior. In contrast, Sylgard 184 and 186 exhibited progressively higher degrees of relaxation, with Sylgard 186 dissipating over 60% of the initial force, indicating pronounced viscoelasticity. A similar trend was found in dynamic mechanical analysis (DMA), in which tan(δ) – the ratio of loss to storage modulus– was measured over a frequency range from 0.5 to 8 Hz (Figure 1C). Sylgard 186 showed the highest tan(δ) values, corresponding to a greater ratio of loss to storage modulus, again confirming that Sylgard 186 was the most viscous substrate. This is followed by Sylgard 184, while QGel 920 is the least viscous of the three elastomers. Comparison of the absolute values of storage and loss moduli supported these findings, as the storage modulus remained comparable, whereas the loss modulus increased according to the viscoelastic behavior (Figure S3, Supporting Information). To confirm that these viscoelastic properties do not have a significant influence on the quantification of the Young’s moduli, additional measurements were performed using the peak load poking mode of the Chiaro nanoindenter, which allows the indentation of the substrates in a shorter timeframe (less than 0.2 s), in which the effects of stress relaxation are minimal. The measurement setup and resulting data are shown in Figure S4 (Supporting Information), and representative displacement and load curves are depicted in Figure S5 (Supporting Information). While the resulting values are slightly lower than those of the conventional measurements (≈69 kPa), no

Table 1. The mechanical properties of the three different substrates used in this study. Reported values represent the mean ± standard deviation (where applicable). The Young's modulus values are based on the measurement shown in Figure 1A to highlight the spread of obtained values within single samples.

Classification	Substrate	Young's modulus [kPa]	Energy dissipation [%]	tan[δ] at 1 Hz
Low SR	QGel 920 (1 to 3)	78.3 ± 1.4	9.4 ± 2.3	0.052 ± 0.005
Med SR	Sylgard 184 (1 to 41)	77.3 ± 1.5	31.5 ± 2.9	0.218 ± 0.015
High SR	Sylgard 186 (1 to 25)	77.1 ± 5.4	61.8 ± 1.5	0.510 ± 0.031

significant differences were found for the three materials, and they do not affect the classification of the substrates as stiff for the cell types used in this study, as the values are still far above what would be considered an intermediate stiffness (≈3 to 5 kPa for selected cell lines).[33]

Given that biological tissues span a wide range of viscoelastic properties,[11] these three materials provide a suitable platform to study how ECM stress relaxation mimicked by artificial substrates influences cell behavior. Together, they offer a mechanically relevant spectrum that mimics the range of viscoelastic properties found in biological tissues, which is consistent with the range reported for many soft and connective tissues, from low stress relaxation (QGel 920) to high stress relaxation (Sylgard 186), with Sylgard 184 being in an intermediate position.[11] This decoupling of stiffness and stress relaxation is especially valuable for investigating time-dependent mechanical cues in the absence of confounding changes in matrix rigidity. Unlike hydrogel-based systems, where stiffness and stress relaxation are often interdependent, the PDMS-based approach used here enables precise tuning of dissipative properties at constant stiffness,

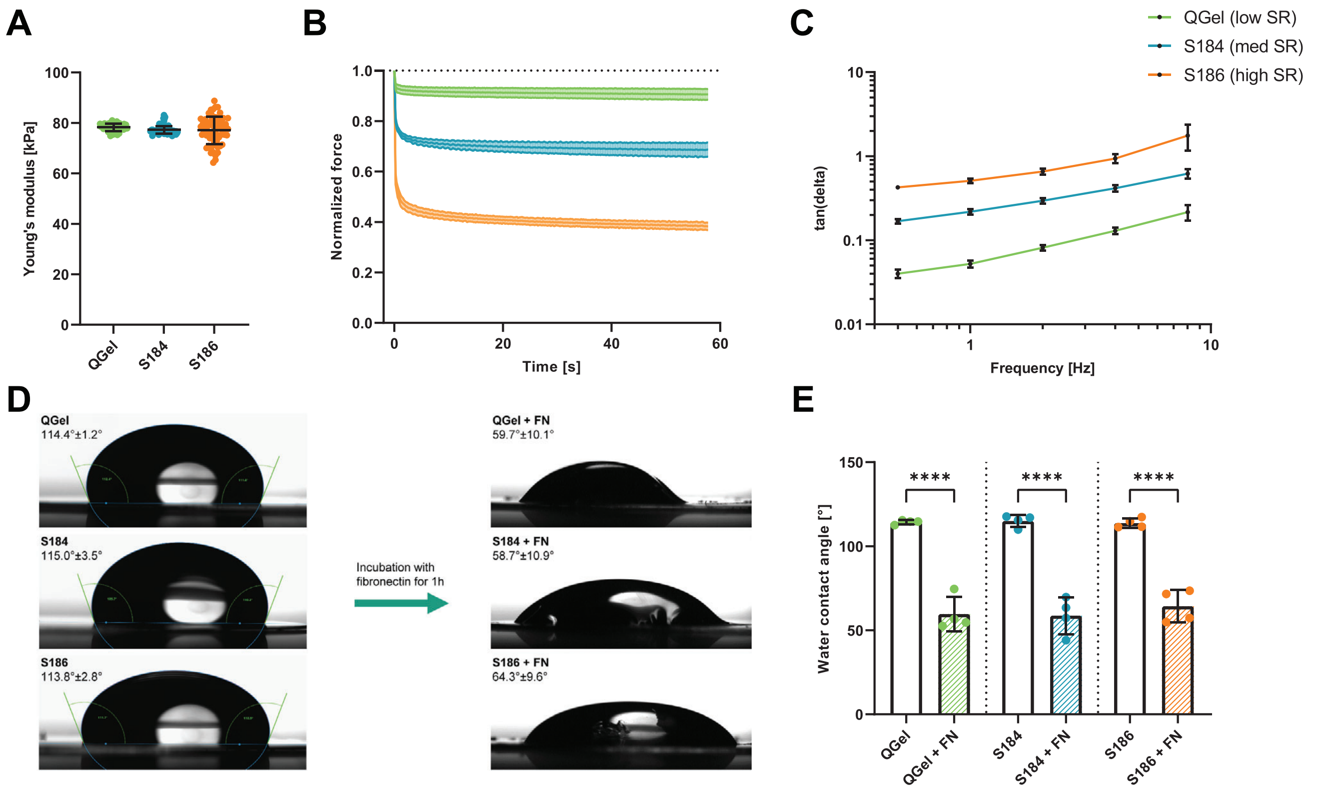

Figure 1. A) Young's modulus measurements for the three different substrates performed using nanoindentation. The data shown here was measured using one sample of each material, and N ⩾ 68 positions were measured. No significant differences between the groups were observed following an ordinary one-way ANOVA with post hoc Tukey. Data are shown as mean values ± standard deviation. The measurements of three separate replicates are shown in Figure S1 (Supporting Information). B) Substrate stress relaxation measurements. The surfaces were indented with a constant indentation depth for 60 s and the average normalized force was calculated for N ⩾ 42 different positions per sample as explained in the methods section. Shown are the means ± standard deviation. C): Tan(delta) measurements of the three substrates in the frequency range from 0.5 to 8 Hz. Loss and storage modulus were obtained through DMA using nanoindentation and the values were divided to calculate the tan(delta). N ⩾ 68 different positions were measured for each frequency and sample, data are shown as mean values ± standard deviation. D) Example images of the water contact angle measurements for the three substrates before and after incubation with FN for 1 h. Contact angles were automatically calculated by the software as can be seen in the example images. E) Water contact angle data for N = 4 different measurements before and after coating of the substrates with FN for 1 h. Shown are the means ± standard deviation. ****: $p < 0.0001$, according to an ordinary one-way ANOVA with post hoc Tukey.

allowing mechanistic dissection of viscoelastic contributions to cell behavior.

To confirm uniform ECM protein coating across all substrates, water contact angle measurements were performed before and after surface coating with the extracellular matrix protein fibronectin (FN) (Figure 1D). All uncoated surfaces were initially hydrophobic, with contact angles exceeding 110°, in agreement with values previously reported for Sylgard 184.[17] After incubation with FN for 1 h and subsequent washing, contact angles decreased to approximately 60° for the three different substrates (Figure 1E), indicating that the coated surfaces were no longer hydrophobic and that the change was due to protein coating.[17,34] The uniform reduction of the water contact angles across the three samples after FN incubation can be taken as the first proof of the homogeneity of the surface coating by the extracellular matrix protein using the proposed protocol.

To further validate the equal coating of the surfaces with FN, and to ensure uniform coating across substrates, immunofluorescence staining was performed using antibodies specific to the FN cell binding domain (**Figure** 2A). Substrates with and without the addition of FN were probed, and fluorescent intensities were measured at various positions on the different surfaces by fluorescence microscopy. Reference images of the coverslip edges were recorded to highlight the contrast between the FN-treated surfaces and the untreated outside within single frames. The background signal of each substrate was recorded using a control without the addition of FN and then subtracted from the fluorescent intensities measured on the coated surfaces. No significant variation was found for the signal of the different substrates, indicating that similar amounts of protein were present on each surface (Figure 2B). It was also observed that with shorter or longer incubation times (0.5 or 2 h), lower or higher levels of FN attachment can be achieved (Figure S6A,B, Supporting Information). This shows that the amount of protein on the surface depends on the duration of the incubation and can be fine-tuned by adjusting the timings, while still resulting in similar levels of FN when comparing the three different substrates. Ultimately, 1 h was chosen as a standard for all other experiments due to the uniformity of the signal, also following previous work conducted using Sylgard 184.[24]

To assess biocompatibility and support for cell growth, HeLa cells were cultured on the three substrates, with tissue culture plastic serving as a reference control surface. Cells were seeded at different densities and left to proliferate for four days before being treated with the alamarBlue Cell Viability Reagent. As an indicator of cell viability, the assay is based on the reduction of resazurin to the highly fluorescent resorufin and the fluorescence intensity of the cell culture medium is measured using a plate reader (Figure 2C).[35,36] For all conditions, fluorescence intensity increased linearly with cell number, indicating that cells were still viable and metabolically active after 4 days. The number of adherent cells was further quantified with a counting chamber after enzymatic detachment with 0.25% Trypsin-EDTA, and no significant differences were detected after 4 days for the different conditions (Figure 2D). Extended cell culture beyond 4 days revealed no adverse effects, and phase-contrast microscopy images after 7 days showed healthy cell morphology on all substrates (Figure S7, Supporting Information). Of note, Sylgard 184 is widely used in many studies and its biocompatibility is well known, as well as its use for various purposes, including mechanobiology studies and the fabrication of microfluidic devices.[17,26,37] In contrast, only very limited information can be found about QGel 920,[28] and Sylgard 186 has not previously been evaluated for cell culture applications, having only been tested as a candidate material for the production of stretchable microfluidic devices.[38] Our results demonstrate that all three materials support cell adhesion and proliferation, validating their use in cell-based assays despite differences in mechanical behavior, and highlight that they can be used for various applications such as fluorescence microscopy, traction force measurements, and the study of cell migration. Therefore, this expands the range of substrates available to study the influence of stress relaxation on cellular behavior by adding silicone based substrates that are easy to use and offer long-term stability, chemical inertness, and the option for integration with other techniques such as soft lithography.

2.2. Substrate Stress Relaxation Regulates Cell Adhesion-Mediated Mechanotransduction

To investigate how stress relaxation of stiff substrate influences cellular adhesion and spreading, HeLa cells were seeded on FN-coated surfaces and fixed after 4 h. Cells were stained with phalloidin and DAPI to visualize the actin cytoskeleton and nuclei (**Figure** 3A). Robust attachment and visible actin stress fibers were observed across all substrate types, consistent with expectations for this cell type adhering to substrates of high stiffness.[24,39,40] Quantification of the cell spreading area revealed a slight albeit not significant decrease in size with increasing substrate stress relaxation (Figure 3B). This observation aligns with previous reports on stiff substrates, where increased stress relaxation is also associated with reduced cell spreading, a pattern that contrasts with behavior on soft substrates (<5 kPa), where stress relaxation enhances spreading.[5,6,41] These findings highlight the importance of time-dependent mechanical feedback in early cell-matrix interactions, even when the overall matrix stiffness remains high. This is particularly relevant for understanding cell behavior in fibrotic or tumor tissues, where ECM remodeling often leads to viscoelastic stiffening.[22,23,42] The full morphological distribution of cell spreading areas can be seen in Figure S8 (Supporting Information), and no qualitative difference was observed comparing the three materials.

Matching the spreading data, cell circularity was found to be lower on the elastic QGel compared to the two viscoelastic substrates after 4 h of attachment (Figure S9, Supporting Information), indicating that the slightly increased spreading area on QGel correlates with more elongated cells. This is in agreement with literature findings for the circularity of cells adhering to substrates classified as stiff for the investigated cells and conditions.[20,41,43] The inverse relationship between cell area and circularity that suggests that larger and more spread cells have a less circular morphology was further supported by time-course experiments, as it was found that cell area increased over time (up to 6 h) as circularity decreased (Figures S10 and S11, Supporting Information).

To further validate the applicability of the substrates in cell culture, the spreading experiments were repeated with NIH 3T3 fibroblasts. Cells were cultured on the FN-coated substrates for

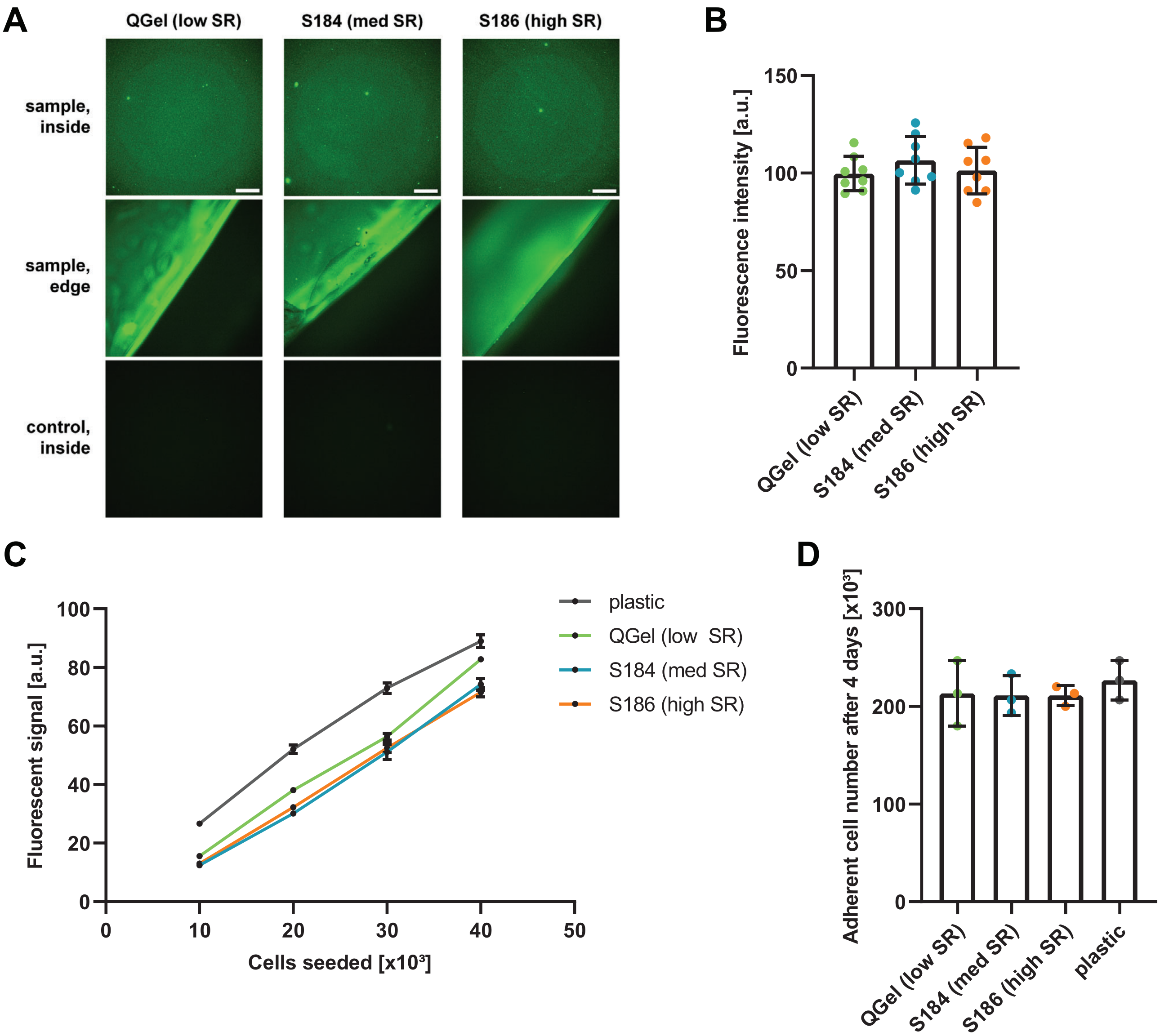

Figure 2. A) Fluorescent microscopy images of FN antibody staining targeting the cell-binding domain. The three different substrates were either coated with FN (here called sample) or uncoated (here called control) before primary and secondary antibody staining. Images inside the sample and control coverslips were taken and are shown with the same brightness and contrast settings. Images of the coverslip edges are included to highlight the difference between FN-coated coverslips and untreated outside in single images. Scale bars equal 100 µm. B) Fluorescent intensities of the FN antibody staining. N = 8 positions were imaged for each sample and the background of the respective control coverslips was subtracted. Shown are the means ± standard deviation. No significant deviation in intensity was observed according to an ordinary one-way ANOVA with post hoc Tukey. C) Fluorescent intensities of the cell culture medium of cells seeded on the different substrates at different starting densities treated with alamarBlue after 4 days in culture. 10, 20, 30, and 40 thousand cells were seeded for 4 days and then incubated with 1× alamarBlue reagent in cell culture medium for 2 h. N = 6 different wells in a 96-well plate filled with 100 µl media were measured at a plate reader for each sample and condition, data are shown as mean values ± standard deviation. D) Cell numbers after 4 days, for the condition with a starting density of 40 thousand cells. Cells were detached with Trypsin-EDTA and counted in a counting chamber for N = 3 separate times. Shown are the means ± standard deviation. No significant variation in cell number was observed according to an ordinary one-way ANOVA with post hoc Tukey for the different substrates.

4 h before fixation and immunofluorescence staining, similar to the HeLa cells, and their spreading area and circularity were analyzed. The same trends were observed, with slightly larger cell spreading areas on the substrates undergoing low stress relaxation, while simultaneously the cell circularity on these substrates was found to be significantly reduced, indicating increased spreading and elongation of cells on the low stress relaxation substrates. Images of the NIH 3T3 cells are shown in Figure S12 (Supporting Information), and the resulting spreading and shape data can be seen in Figure S13 (Supporting Information).

To investigate how stress relaxation modulates mechanotransduction, YAP1 localization was evaluated as a readout for adhesion-mediated signaling. Cells were fixed after 4 h of

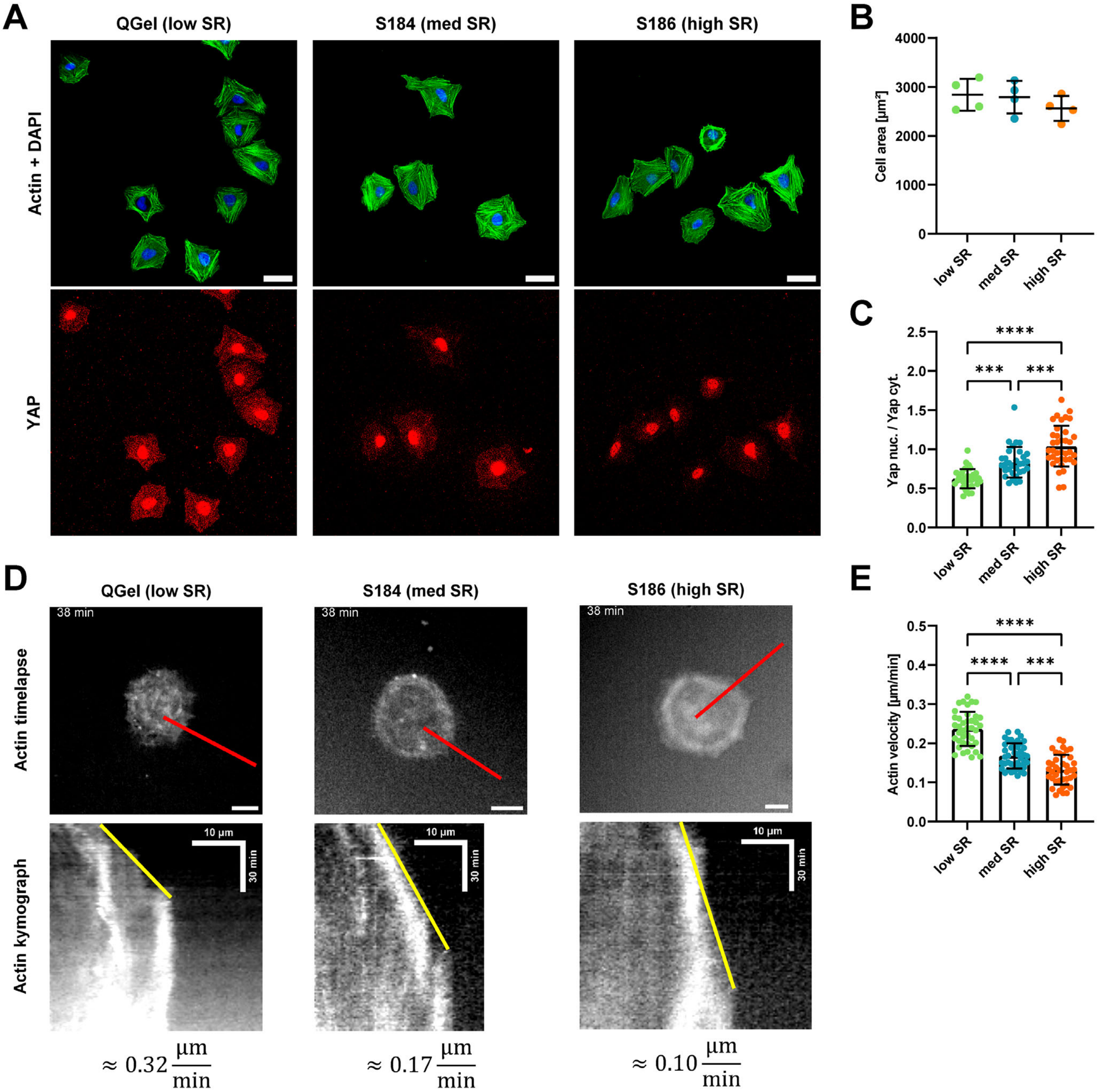

Figure 3. A) Fluorescent microscopy images of HeLa cells fixed after 4 h of attachment. Cells were stained with phalloidin for actin, DAPI for the nuclei (both top row), and antibodies for YAP (bottom). The scale bars represent 50 µm. B) Cell spreading area measured after 4 h based on cellular actin staining. Results of four separate experiments with N > 300 each, data are shown as mean values ± standard deviation¨ C) Ratio of nuclear to cytosolic YAP measured in cells. Images of YAP were taken after fixation and immunofluorescence staining of the cells. N ⩾ 32 for each sample, with each data point representing one cell. Shown are the means ± standard deviation. ***: $p < 0.001$, ****: $p < 0.0001$, according to an ordinary one-way ANOVA with post hoc Tukey. D) First frames of the actin time lapse videos recorded using fastAct for HeLa cells seeded on the different substrates. Scale bars correspond to 10 µm. Red lines represent the positions selected to create the actin kymographs that are shown below the cell images. Yellow lines show the linear fits selected to calculate the actin velocities, with the respective values shown as examples underneath. E) Actin velocity data measured using the time lapse videos for the different substrates. N ⩾ 40 cells and kymographs were measured for each sample. Data are shown as mean values ± standard deviation. ***: $p < 0.001$, ****: $p < 0.0001$, according to an ordinary one-way ANOVA with post hoc Tukey.

attachment, and YAP1 immunostaining was performed. The nuclear-to-cytosolic YAP1 ratio was quantified for each cell (Figure 3A, C). Cells on substrates undergoing higher stress relaxation showed elevated nuclear YAP1 ratios, indicating reduced cytosolic localization. This trend is consistent with previous reports on substrates with stress-relaxation properties,[5,19] although the findings vary depending on cell type and substrate formulation.[20,43] Importantly, none of these studies was carried out in the stiffness regime (≈80 kPa) used in our work. The elevated YAP nuclear localization on substrates with higher stress relaxation implies that it facilitates sustained tension and/or nuclear deformation over time, possibly via increased adhesion. It also suggests that cells interpret viscoelasticity not as "softness" but as a unique mechanical input that modulates force loading and cytoskeletal dynamics.

To capture early cytoskeletal dynamics, live-cell imaging of actin during cell spreading was performed using the SPY555-FastAct probe, starting approximately 30 min after cell seeding. Time-lapse movies were used to generate actin kymographs for individual cells, allowing the measurement of spreading velocity over the first 2 h by fitting the linear portion of the actin signal in the kymographs (Figure 3D). Cells were found to spread faster on low stress relaxation substrates, with an average actin velocity of (0.24 ± 0.04) µm min^{-1} on QGel (Figure 3E). On the medium SR Sylgard 184 the velocity was (0.17 ± 0.03) µm min^{-1} and on the high SR Sylgard 186 (0.13 ± 0.04) µm min^{-1}. These results support observations made for cells fixed at different time points (Figures S10 and S11, Supporting Information) since larger cell spreading areas were also found at early time points (1.5 to 3 h) on low SR substrates, with differences diminishing later on (6 h after seeding). Together, these results suggest that substrate elasticity enhances early cellular spreading dynamics while stress relaxation slows cytoskeletal remodeling. This is consistent with reports showing that increased substrate stress relaxation has a negative effect on both spreading and migration behavior in the stiff regime.[5,20] Future studies will be needed to determine how substrate stress relaxation behavior specifically influences single cell and cell collective migration, and in particular regulates cell-matrix and cell–cell adhesion dynamics.

2.3. Substrate Stress Relaxation Regulates Focal Adhesion Architecture and Integrin-Dependent Matrix Organization

To determine how substrate stress relaxation influences focal adhesion assembly, cells were fixed 4 h after seeding and stained for vinculin. Single-cell fluorescence images revealed differences in adhesion morphology across substrates with varying stress relaxation properties (**Figure 4**A). Quantitative image analysis showed that focal adhesions were larger in area for cells adhering to substrates of higher stress relaxation. A higher percentage of focal adhesions with an area above 2.5 µm^2 was found in these cells, while a larger ratio of small focal adhesions below 1 µm^2 was found on the elastic substrate (Figure 4B). The average focal adhesion area per cell increased with increasing stress relaxation, being (1.45 ± 0.26) µm^2 on the low SR QGel (1.72 ± 0.18) µm^2 on the med SR S184, and (2.03 ± 0.15) µm^2 on the high SR S186 (Figure S14A, Supporting Information). A similar trend was observed for focal adhesion number per cell (Figure S14B, Supporting Information), indicating that stress relaxation promotes both maturation and increased density of adhesion sites. For increased clarity of the scope of the data the total distributions of focal adhesion area and length are shown in Figure S14C,D (Supporting Information). Notably, focal adhesions on the low SR substrate QGel were predominantly located at the cell periphery, while the substrates undergoing higher stress relaxation S184 and S186 induced the formation of adhesions toward the cell center. This shift in spatial organization suggests the emergence of fibrillar adhesions, which are known to form centrally by the translocation of integrins from peripheral adhesions and sustained tension.[44] This redistribution of adhesions from peripheral to central zones strongly suggests a shift in force balance and integrin recycling behavior, both of which are known to contribute to fibrillar adhesion maturation.[45] Such reorganization has been associated with increased actomyosin contractility and a switch in adhesion dynamics from nascent to stable structures, particularly under conditions of prolonged force loading.[46] It is likely that enhanced stress relaxation facilitates sufficient time-dependent tension to promote this transition.

To further dissect integrin-specific contributions, cells were also stained for β1 and αvβ3 integrin. To visualize matrix remodeling, FN conjugated with HiLyte Fluor 647 was used to coat the substrates, enabling direct observation of FN rearrangement during cell adhesion on the different substrates (Figure 4C). Marked differences in FN distribution were found between the samples: on substrates undergoing higher stress relaxation, FN appeared reorganized into elongated "fibrillar-like" structures in close proximity to focal adhesions, whereas low SR QGel surfaces showed a more diffuse FN signal.

High-resolution imaging revealed that β1 integrins colocalize with FN fibrils, often at the end of actin stress fibers (Figure 4D). Quantitative colocalization analysis confirmed a stress relaxation-guided increase in integrin-FN coupling, since the Pearson correlation coefficient rose from 0.161 ± 0.069 on low SR QGel to 0.328 ± 0.130 on med SR S184 and 0.331 ± 0.124 on high SR S186 (Figure 4E), in alignment with the observations of enhanced matrix remodeling on stress-relaxing substrates. While αvβ3 integrin was also detected at adhesion sites, no significant differences in distribution were observed across the different substrates (Figure S15, Supporting Information), suggesting a more prominent function of β1 integrin in mechanosensitive FN remodeling on the substrates. This preferential involvement of β1 integrins is consistent with their known role in fibronectin fibrillogenesis, where they mediate traction-dependent matrix assembly.[47,48]

Our data suggest that substrate stress relaxation amplifies the force transmission through β1 integrins necessary to drive FN remodeling, independent of stiffness or ligand density. The lack of response from αvβ3 integrins may reflect their lower force sensitivity or distinct activation threshold in comparison to β1 integrins under dynamic mechanical conditions.[49] Taken together, these findings indicate that stress relaxation promotes the spatial reorganization and mechanical engagement of integrins critical for ECM remodeling, and an activation threshold might exist that is already reached with the substrates undergoing intermediate stress relaxation. It would be interesting in future work to test whether inhibition of β1 integrin blocks the observed FN rearrangement to causally link the observed correlation with

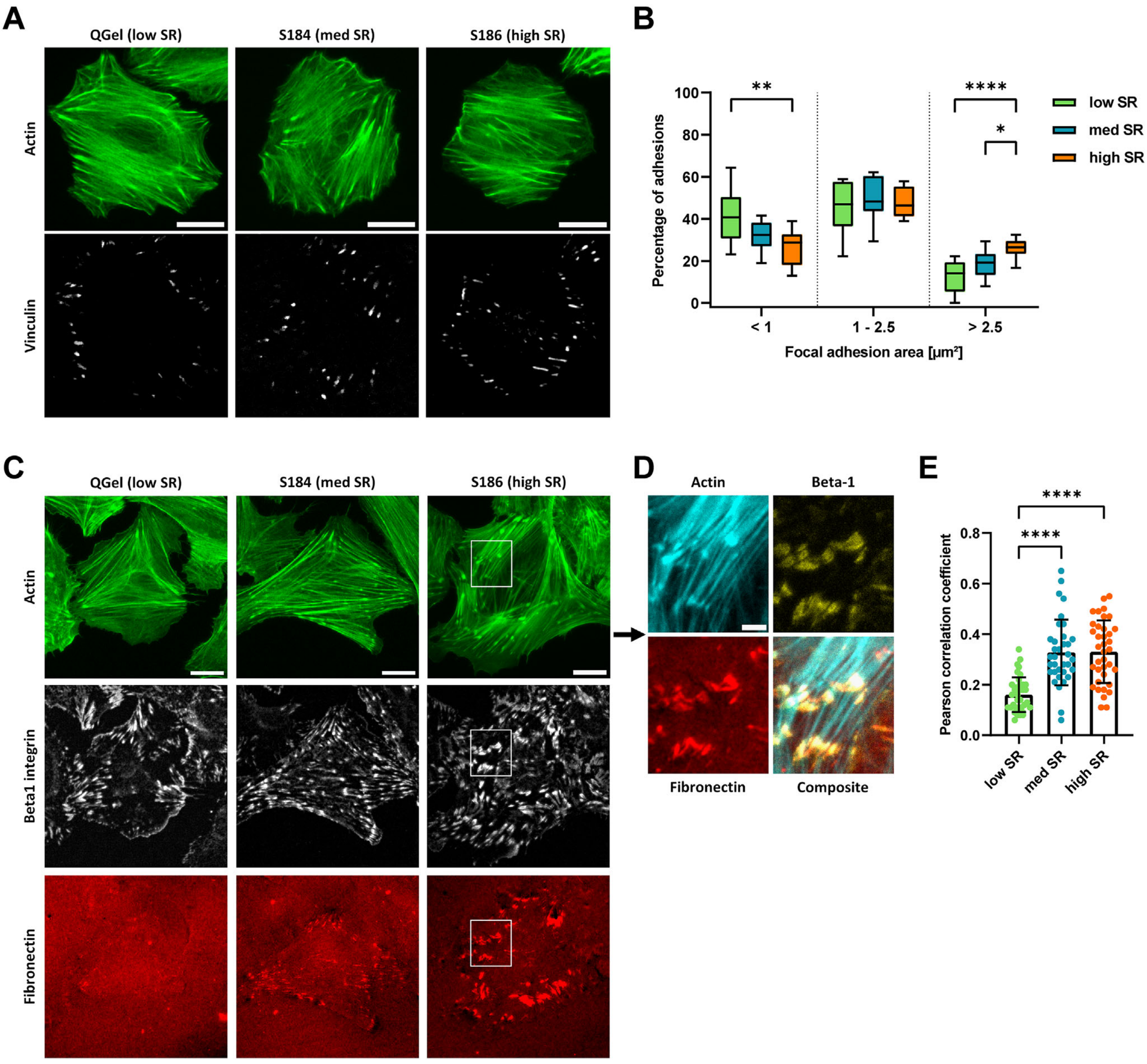

Figure 4. A) Fluorescence microscopy images of HeLa cells fixed and stained after 4 h of attachment to the different substrates. Cells were stained for actin using phalloidin, and an antibody staining was performed to image cellular vinculin. Scale bars equal 20 µm. B) Percentage of vinculin focal adhesions per cell on the different substrates sorted by size into three categories. N ⩾ 10 cells were analyzed for each substrate, and the ratio of focal adhesions that fall in each category was calculated per cell. A box plot with whiskers was chosen for increased clarity. The box represents the 25th to 75th percentiles, the whiskers indicate the min and max, and the line is the median of the respective sample. *: $p < 0.05$, **: $p < 0.01$, ****: $p < 0.0001$, according to an ordinary one-way ANOVA with post hoc Tukey performed for each size category. C) Fluorescence microscopy images of HeLa cells fixed after 4 h of attachment. Actin was stained with phalloidin, and beta-1 integrin and fibronectin images were recorded after immunostaining. Scale bars correspond to 20 µm. D) Zoom in to the marked area of the S186 image of Figure 4D. Actin, beta-1 integrin, and fibronectin structures can be observed more closely, and the three channels' composite image is shown. The scale bar equals 5 µm. E) Pearson correlation coefficient measured for cellular beta-1 integrin signal and underlying fibronectin. The correlation underneath the cell area was measured for N ⩾ 35 cells after the cellular outline was created based on the corresponding actin images. Data are shown as mean values ± standard deviation. ****: $p < 0.0001$, according to an ordinary one-way ANOVA with post hoc Tukey.

functional remodeling. How different ECM proteins and integrin subtypes influence cell adhesion could also represent an important direction to determine whether the observed adhesion responses depend on matrix specific interactions and whether ECM remodeling is essential for these.

2.4. Cellular Traction Correlates with Fibronectin Reorganization at Adhesion Sites

The assembly of a fibrillar FN matrix requires cells to exert contractile forces that stretch FN molecules, exposing cryptic

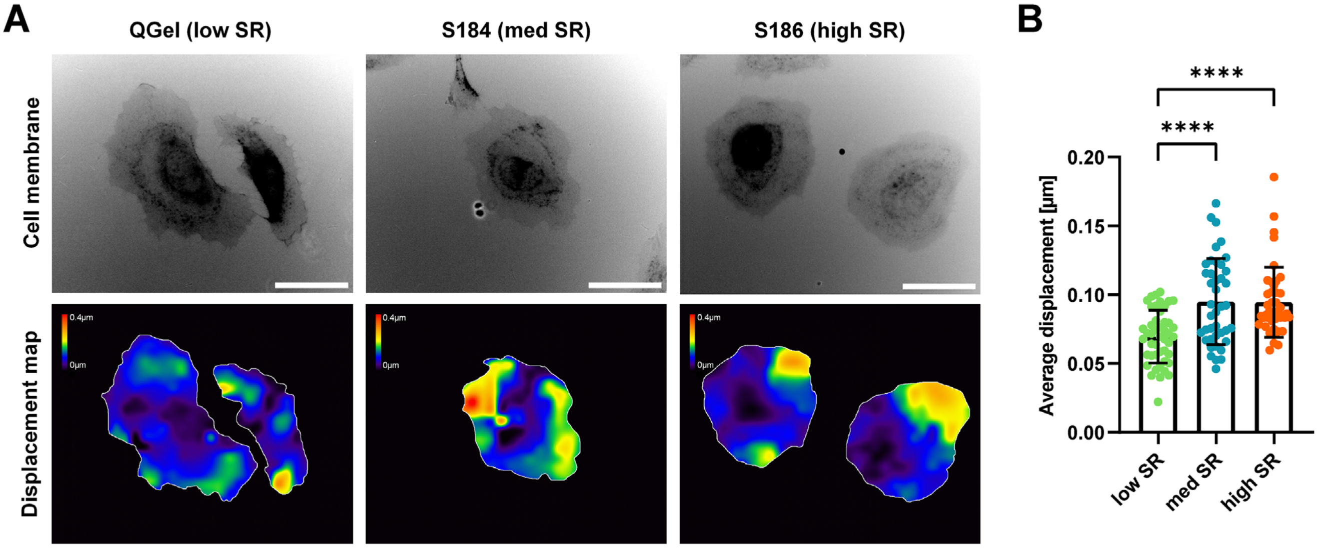

Figure 5. A) Traction force microscopy images. The top row shows images of cells stained using a WGA membrane dye and the bottom row the corresponding displacement maps calculated based on the movement of the fluorescent nanoparticles covalently bound to the substrate surfaces. The cell outlines were created based on the membrane staining images and were used for the calculation of the average displacement per cell. Scale bars represent 40 µm. The color scaling of the displacement maps is the same for all three images. B) Traction force microscopy data. Average displacements were calculated for each cell using the displacement maps and the cell outlines. $N \geqslant 41$ cells were measured for each sample. Shown are the means ± standard deviation. ****: $p < 0.0001$, according to an ordinary one-way ANOVA with post hoc Tukey.

self-association sites necessary for fibrillogenesis.[32,50] To evaluate how stress relaxation modulates cell-generated forces, traction force microscopy (TFM) was performed on the low, medium, and high SR substrates. Here, fluorescent nanoparticles were covalently bound to the different substrates before FN coating (Figure S16, Supporting Information), allowing for the quantification of cell-induced displacements after 4 h of adhesion (**Figure 5A**). On low SR QGel, the average bead displacement induced by cells was 0.070 ± 0.019 µm, while on medium and high SR S184 and S186, it was 0.095 ± 0.031 and 0.095 ± 0.025 µm, respectively (Figure 5B). This corresponds to an approximate 36% increase in displacement, suggesting that stress relaxation facilitates stronger and more sustained mechanical engagement with the substrate.

Due to the time-dependent mechanical behavior of viscoelastic materials, conventional traction force calculations based on linear elasticity are not valid for the study presented here.[51,52] Instead, displacement magnitude was used as a proxy for cell-generated forces. While this limits force quantification, it still provides a robust comparison between the different conditions. Interestingly, lower traction forces on substrates of higher stress relaxation were reported when using conventional TFM approaches,[19,41,43] potentially due to reference images only being taken after cell removal or differences in substrate stiffness employed in the respective studies. In our case, using displacement data captured before cell adhesion and on relatively stiff substrates, we observe the opposite trend. These contrasting findings underscore the importance of experimental timing and mechanical regime in interpreting TFM data. In particular, our results suggest that under high-stiffness conditions, stress relaxation does not dissipate force but instead permits more effective substrate engagement by cells. This may reflect a shift in cell mechanosensing where delayed relaxation enables more efficient force buildup before feedback inhibition mechanisms are triggered. Taken together, our results indicate that stress relaxation not only alters focal adhesion morphology and integrin-FN interactions but also enhances substrate deformation, likely promoting conditions that favor FN matrix reorganization. While we cannot conclusively demonstrate the formation of mature fibrillar FN from these data, the elongation and spatial alignment of FN with $\beta 1$ integrins and actin stress fibers strongly suggest active mechanical remodeling of the matrix.[47,48] This is particularly notable because the observed FN structures form without any additional biochemical stimulation, indicating that stress relaxation alone can trigger cell-driven reorganization of ECM proteins. Future work could explore whether inhibition of actomyosin contractility or $\beta 1$ integrin engagement prevents this remodeling, further clarifying the causal relationship between substrate mechanics, traction force generation, and matrix assembly.

In summary, the findings presented here highlight a broader conceptual contribution of our study: by decoupling viscoelasticity from stiffness, we establish a material-based platform to investigate how time-dependent mechanical properties alone regulate ECM remodeling by cells. Through the combination of traction displacement analysis, integrin colocalization with ECM proteins, and dynamic cytoskeletal measurements, our approach provides a multidimensional view of mechanosensitive matrix assembly. This enables systematic quantification of biophysical outputs under controlled mechanical conditions and serves as a foundation for future integration with transcriptomic or proteomic analyses to dissect downstream signaling pathways.

3. Conclusion

In this work, three distinct silicone-based substrates were introduced that can be used to mimic the mechanical properties of the extracellular matrix to study the influence of ECM stress relaxation on cell behavior in the stiff regime. The mechanical properties of the substrates were quantified and it was verified that they significantly differ in their stress relaxation behavior while having similar stiffness, a crucial condition for isolating the effects of stress relaxation from stiffness-dependent responses. Using HeLa cells, it was further validated that the substrates do not exhibit cytotoxicity and are suitable for cell culture. Uniform FN coating was confirmed via antibody staining and fluorescence imaging, indicating that the substrates can be functionalized reproducibly with ECM proteins.

The influence of substrate stress relaxation on cellular mechanosensing was investigated by quantifying the localization of YAP within the cells, and a significantly higher ratio of nuclear to cytosolic YAP was found on low SR substrates. This suggests enhanced activation of mechanosensitive signaling pathways in response to time-dependent mechanical properties. HeLa spreading area and shape were measured after 4 h of attachment, and actin dynamics during initial spreading were quantified. Cells were found to be slightly larger on low SR substrates, and higher actin velocities were measured compared to the more viscous substrates, indicating that stress relaxation delays cytoskeletal engagement and slows the spreading process during early adhesion.

Cellular focal adhesion formation was studied based on antibody staining for vinculin, and larger and longer adhesions were found on more viscous substrates, particularly the high SR substrate. When fluorescently labeled fibronectin was used to coat the surfaces, it was subsequently revealed that cells on the more viscous substrates were remodeling the fibronectin layer creating FN-enriched agglomerations, with strong colocalization of these fibronectin structures with $\beta 1$ integrins.[47,48] This spatial alignment of integrin, FN, and actin suggests a stress relaxation-driven maturation of adhesion structures and remodeling of the ECM. Traction force measurements showed a similar trend, with larger average displacement on the medium and high SR substrates, indicating increased cell-substrate force transmission that may be required to mechanically unfold FN dimers and initiate the process of fibrillogenesis.[32,50]

Together, these findings demonstrate that substrate stress relaxation independent of stiffness is central in regulating cellular force generation, adhesion maturation, and matrix remodeling. Our study highlights the utility of tunable viscoelastic materials for dissecting mechanoresponsive cell behavior and provides a framework for designing next-generation biomaterials that incorporate time-dependent mechanical cues to guide tissue organization.

The results presented in this work were obtained using a targeted imaging-based approach to capture early structural and mechanical responses of cells to substrate viscoelasticity. While limited to a single time point, our study provides a necessary first step toward understanding how time-dependent mechanical cues regulate cell behavior. We believe that these findings lay the groundwork for future mechanistic dissection using transcriptomic or proteomic approaches, particularly in time-course studies designed to capture the evolution of downstream mechanosensitive signaling. Expanding this model to include additional ECM proteins beyond FN will also be important to assess matrix-specific effects. Ultimately, integrating biochemical analyses with dynamic profiling and collective cell behaviors will be key to advancing a comprehensive understanding of viscoelastic regulation in complex cellular systems.

4. Experimental Section

Substrate Production: The three substrates were prepared by carefully weighing the two components of each using a precision balance, after which they were thoroughly mixed and then degassed using a desiccator. For cell viability experiments, approximately 1.5 ml of each substrate was poured into the wells of six-well plates to create entire wells covered with the substrates. For microscopy experiments, 25 mm coverslips (Carl Roth, 1.5H) were first cleaned in a UV-Ozone cleaner (Jelight Company) for 10 min before spin coating (Laurell Technologies, WS-650) at 5000 rpm for 10 s. After this, the substrates were cured and stored before use according to **Table 2**. Particularly for the Sylgard 184 substrates, a minimum storage time was set because it was noticed that the substrates seemed to undergo further hardening after initial curing, which had also been reported elsewhere.[25] Substrates were therefore only used for experiments after storage for a minimum amount of time, when the hardening seemed to have reached a plateau.

Substrate Characterization: The mechanical properties of the substrates were measured using a Chiaro nanoindenter from Optics11 Life mounted on the stage of a Nikon Ti2 Eclipse inverted microscope. Before the measurements, substrates were incubated with a 1% (w/w) solution of bovine serum albumin (BSA, Sigma–Aldrich, A2153-50G) in PBS for 1 h at room temperature, to reduce sticking of the nanoindenter probe to the substrates, which could otherwise have disturbing effects on longer and repeated measurements. A probe with a radius of 24 µm and stiffness of 0.23 N m^{-1} was used to record matrix scans of the substrates with 9×9 positions spaced 200 µm apart. The probe was positioned 2 µm above the substrate surfaces using the integrated find surface function before each measurement and lowered by 10 µm in 2 s using the displacement control mode of the nanoindenter to record stress displacement curves. The Young's modulus was then calculated for each measurement using the Hertzian contact model to fit the elastic region of the loading curves (Figure 1A). Three different substrates were prepared for each substrate type and measured to validate the consistency of the manufacturing process (Figure S1, Supporting Information). The influence of surface coating with proteins on the stiffness measurements was investigated for Sylgard 184 in the past using fibronectin, and no significant difference was found when indenting either uncoated or FN-coated surfaces.[24]

The substrates' tan(δ) was measured using the same matrix scans (Figure 1C). For this, after the initial indentations, while the probe was still in contact with the substrates, 20 s were waited to give the substrates time for initial relaxation. After that, the DMA mode (dynamic mechanical analysis) of the nanoindenter was set to indent the substrates for an extra 1 µm, with oscillations at different frequencies ranging from 0.5 to 8 Hz with 5 periods each. From this, the load and storage moduli were also calculated (Figure S2, Supporting Information).

A second matrix scan of similar size was performed to measure the stress relaxation of the substrates, this time using the indentation control mode. The tip was again brought 2 µm above the surfaces, and a time of 0.2 s was set for the nanoindenter to reach a stable indentation depth of 2 µm, at which the head remained for 60 s. During this time, the necessary load to keep the indentation constant was recorded, normalized, and averaged to create the stress relaxation curves (Figure 1B). Data processing for this was performed using software available on GitHub.[53]

To validate that substrate stress relaxation has no significant effect on the obtained stiffness values additional measurements were conducted using the peak load poking mode of the Chiaro nanoindenter (Figure S4B, Supporting Information). Substrates were indented up to a maximum load of 1 µN with a Piezo speed of 30 µm s^{-1} with typical indentations taking less than 0.2 s (Figures S4A and S5, Supporting Information). A matrix scan of 6×6 positions with a spacing of 600 µm was conducted to measure a large area on the surfaces.

Table 2. Mixing ratios and curing schedules for the different substrates.

	QGel 920	Sylgard 184	Sylgard 186
Mixing ratio	1 to 3 (A to B)	1 to 41 (Curing agent to base)	1 to 25 (Curing agent to base)
Curing time	overnight	overnight	3h
Curing temperature	room-temperature	70 °C	70 °C
Minimum storage time	2 days	14 days	none

Water contact angle measurements were performed using a drop shape analyzer (DSA25, Krüss). Coverslips spin-coated with the different substrates were placed in front of the camera, and a 150 µl drop of milli-Q water (Merck) was placed in the center. After focusing, the software automatically calculated the contact angles of the left and right sides. Both were averaged, and a total of four different measurements were performed for each sample, either for plain uncoated coverslips or after coating with fibronectin for 1 h (Figure 1D,E). Contact angles were measured immediately after droplet deposition without any additional waiting time. No significant change in angles was observed during the measurement of single samples.

Fibronectin Coating and Validation of Coating Homogeneity: Substrates were coated using fibronectin from bovine plasma (Sigma–Aldrich, F1141) by diluting the protein in phosphate-buffered saline (PBS, Thermo Fisher Scientific, 10010023) to a final concentration of 3.34 µg ml^{-1} and incubating the surfaces with the solution for 1 h at room temperature. The coating-concentration was based on previous work using Sylgard 184, and was fine-tuned for optimized results when culturing HeLa cells.[24] After this, the surfaces were washed three times with PBS to remove excess FN. To validate the surface coating (Figure 2A, B; Figure S3, Supporting Information), the substrates were incubated with a 1% solution of BSA in PBS for 1 h at room temperature before another three washing steps. Then an anti-fibronectin mouse antibody targeting the cell-binding domain of human and bovine fibronectin (QED Bioscience, 42040) was added at a concentration of 10 µg ml^{-1} in 1% BSA in PBS for 1 h at room temperature. After three washing steps, the goat anti-mouse secondary antibody Alexa Fluor 488 (Invitrogen, A-11001) was added at a concentration of 4 µg ml^{-1} in 1% BSA in PBS for 1 h at room temperature. The coverslips were then washed a final three times and mounted on glass slides with 40 µL of Mowiol 4-88 (Carl Roth, 0731.2). For the negative control samples, the same steps were performed except for the substrate coating with fibronectin in the beginning. Uniform surface coating with FN across the different substrates was then quantified using fluorescence microscopy and taking this together with the consistent wettability changes, similar levels of the ECM protein on the different surfaces were concluded.

To investigate the influence of different incubation times, tests were also conducted where the FN solution was added for 0.5, 1, or 2 h for surface coating. The incubation time of 1 h was selected for all of the experiments as the optimal condition where all substrates reached the same levels of surface-bound FN and follows previous work conducted using Sylgard 184 at different mixing ratios.[24]

Cell Culture: HeLa cells were used for all experiments and cultured at 37 °C with 5% CO_2 using DMEM high glucose GlutaMAX (Gibco, 10566016) supplemented with 10% fetal bovine serum (FBS, Sigma–Aldrich, F7524) and 1% penicillin-streptomycin (P/S, Gibco, 15140-122). To detach cells for experiments, they were washed once with PBS and then incubated with 0.05% of Trypsin-EDTA (Gibco, 25300062) for 5 min. Cells were then washed off the culture flask using fresh medium and centrifuged for 5 min to form a pellet before being resuspended in fresh medium and used for experiments.

NIH 3T3 mouse fibroblasts were used for further validation of the usability of the substrates in cell culture and were cultured in the same conditions as the HeLa cells with the culture medium DMEM (Gibco, 41966029) supplemented with 10% heat inactivated FBS (Gibco, 10082147) and 1% P/S.

Cell Viability: Cell viability was confirmed using the alamarBlue cell viability reagent (Invitrogen, DAL1100). Cells were cultured on the different substrates coated with fibronectin and on tissue culture-treated plastic at different seeding concentrations for 4 days. They were counted using a hemocytometer, and 10000, 20000, 30000, or 40000 cells were seeded per well. After 4 days, the culture media was exchanged with 1 mL of fresh media containing 10% alamarBlue, and cells were left to incubate with the reagent for 2 h. The media was then transferred to a 96 well-plate, and 100 µL of media was added to each well, with six wells for each sample and concentration. The fluorescent signal at four different positions in each well was then measured and averaged in a plate reader with an excitation wavelength of 555 nm and an emission wavelength of 600 nm with filter bandwidths of 20 nm (Figure 2C). Cells in the well where 40000 cells were seeded were then detached using 0.25% of Trypsin-EDTA, and each sample was counted three times to calculate the total number of cells per sample after 4 days of attachment (Figure 2D).

Fluorescent Staining: To perform immunofluorescence imaging, cells were typically fixed after 4 h of attachment on the substrates using 4% paraformaldehyde (PFA, Carl Roth, 0335.1). First, the culture media was removed, and cells were washed once using PBS. After that, PFA was added for 10 min at room temperature. After another three washes with PBS, cells were incubated with 0.1 % Triton X-100 (Sigma–Aldrich, X100RS-25G) in PBS for 5 min at room temperature and washed three times with PBS. Cells were then incubated with 1 % BSA in PBS for 1 h at room temperature before washing three times with PBS and incubation with 0.1 % Triton for 5 min followed by another three washing steps with PBS. Primary antibodies were then added in a 1 % solution of BSA in PBS as detailed below.

To image actin fibers, either phalloidin conjugated with fluophores (see below) or VECTASHIELD HardSet Antifade Mounting Medium with Phalloidin TRITC (Vector Laboratories, H-1600-10) was used. For conjugated phalloidin, a concentration of 1 µM in a 1% solution of BSA in PBS was added to the cells for 1 h at room temperature. For Vectashield, actin was stained after coverslips mounting, as the mounting media contained phalloidin. Note that in this case, the signal-to-noise ratio was less optimal, as excess fluorescent proteins would not be washed away after staining. However, for most of the purposes in this work, the resulting images still allowed subsequent analysis.

For the YAP1 images (Figure 3A), YAP1 (63.7) mouse antibody (Santa Cruz Biotechnology, sc-101199) was added overnight at 4 °C at a concentration of 1 µg ml^{-1} diluted in 1% BSA in PBS. After incubation, cells were washed three times using PBS and incubated with 0.1% Triton X-100 for 5 min before another three washing steps. Then, cells were incubated with goat anti-mouse Alexa Fluor 647 secondary antibody (Invitrogen, A-21236) at 2 µg ml^{-1} in 1% BSA in PBS for 1 h at room temperature. For the nuclear staining in the YAP1 images (Figure 3A), DAPI (4',6-diamidino-2-phenylindole, ROTH, 6335.1) was used at a concentration of 1 µg ml^{-1} and was added alongside the secondary antibody. Coverslips were washed three times using PBS and mounted using 40 µL of Mowiol 4-88 each.

For vinculin images (Figure 4A), similar steps were performed except that instead of YAP1 primary antibodies, anti-vinculin mouse antibodies (Sigma, V9131) were diluted 1 to 100 in 1% BSA in PBS and added to cells for 2 h at room temperature. Samples were then washed three times using PBS, and 0.1 % Triton X-100 was added for 2 min. Cells were washed another three times using PBS and incubated with goat anti-mouse Alexa Fluor 647 secondary antibody (Invitrogen, A-21236) at 4 µg ml^{-1} in 1% BSA in PBS for 2 h at room temperature. After three washes with PBS,

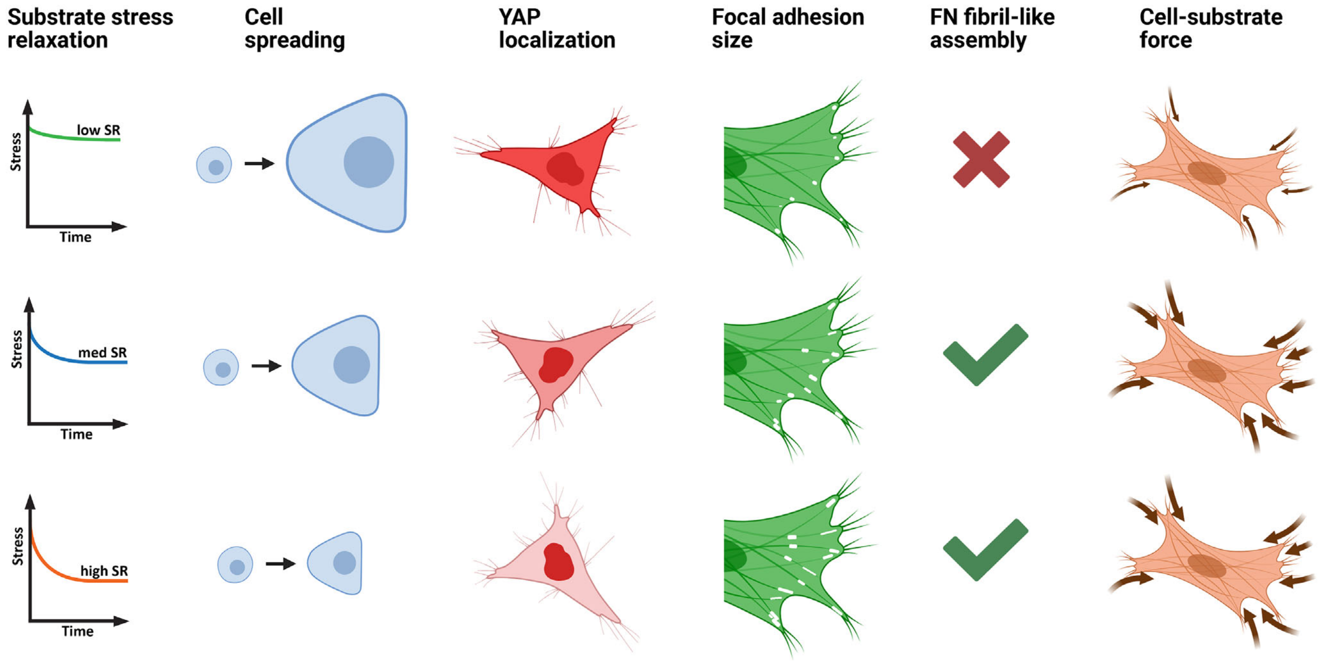

Figure 6. Overview cartoon showing the results of the different experiments conducted using the three substrates. Created in BioRender. Voigt, J. (2025) https://BioRender.com/w56k779.

the coverslips were mounted using Vectashield Mounting Medium with phalloidin TRITC.

For integrin staining (Figure 4C, D), Far-red HiLyte Fluor 647 Labeled Fluorescent Fibronectin (Cytoskeleton Inc, FNR04) was used to coat the surfaces. The fibronectin was diluted to 1.67 µg ml^{-1} in PBS, and coverslips were incubated for 1 h at room temperature, followed by overnight incubation at 4 °C. After three washing steps with PBS, cells were seeded for 4 h, fixed with PFA, and permeabilized with Triton X-100 as described above. Then, anti-integrin beta one mouse antibody (Abcam, ab30394, clone 12G10) was used at a concentration of 10 µg ml^{-1} diluted in 1% BSA in PBS. For $\alpha v\beta 3$ integrin staining (Figure S9, Supporting Information), anti-integrin $\alpha v\beta 3$ mouse antibody (Millipore, MAB1976, clone LM609) was used instead, at a concentration of 10 µg ml^{-1} diluted in 1% BSA in PBS. The antibodies were added to the coverslips for 1 h at room temperature. After, coverslips were washed three times using PBS, and 0.1% Triton X-100 was added for 2 min. After three washing steps with PBS, goat anti-mouse secondary antibody Alexa Fluor 488 (Invitrogen, A-11001) was added at a concentration of 4 µg ml^{-1} in 1% BSA in PBS for 1 h at room temperature. Also, phalloidin Alexa Fluor 555 conjugate (Invitrogen, A34055) was added alongside secondary antibodies at a concentration of 1 µM. After staining, coverslips were again washed three times using PBS and mounted using 40 µL of Mowiol 4-88 each.

Image Acquisition: A Nikon Ti2 Eclipse epifluorescent inverted microscope was used to take fluorescent images of cells and nanoparticles and to take time-lapse videos with the GFP, Cy3, or Cy5 filters and channels of the microscope, depending on the wavelengths of the fluorophores used. A 20× air objective (S Plan FLUOR ELWD, NA 0.45) was used to take images of FN surfaces, quantify cellular spreading area, and conduct the time-lapse study of cellular spreading dynamics. In the case of size quantification, large 3 × 3 images were taken and stitched using the built-in function of Nikon software NIS-Elements to image a large number of cells with high resolution. A 40× air objective (S Plan Fluor ELWD, NA 0.60) was used to take images of fixed cells stained with various antibodies and to image the cells and nanoparticle layers used for traction force microscopy. In the case of the vinculin and integrin images, an additional zoom of 1.5× was set for the microscope for an effective magnification of 60×. Generally, 200 ms of exposure time were set using 20% light intensity, with the exception of the FN and vinculin images, were longer exposure times of up to 4 s were used to increase the signal intensity of the resulting images.

For the YAP analysis an inverted laser scanning confocal microscope (Zeiss Axio Observer Z1, LSM880) equipped with a 20× air objective (Plan-Apochromat, NA 0.8) was used with the following laser settings for imaging: 405 nm 30% (DAPI), 561 nm 20% (TRITC), and 633 nm 5% (AF-647).

For the NIH 3T3 images in the supporting information an epifluorescent inverted microscope with a 40× air objective (Plan Apo DIC, NA 0.95) was used with a GFP filter and 100 ms of exposure. Large images were taken as before and stitched using the Nikon software NIS-Elements to be used for size and shape quantification.

Cell Size and Shape: To analyze cell size and shape, Cellpose[54,55] (version 2.2.3) was used. Cells were cultured on the FN-coated substrates for 4 h and subsequently fixed and stained for actin using phalloidin as detailed in the previous subsection. Images were opened in the GUI of Cellpose and cells were outlined using the cyto model of the software after an appropriate cell diameter was set based on the pixel size of the images. Faulty outlines were corrected by hand to improve the model performance and a custom model was trained using the human-in-the-loop pipeline.[55] The masks were saved as imageJ ROI files, opened in Fiji,[56] and analyzed using the measurement function to quantify the area and shape of the cells based on the outlines.

YAP Localization: Cells were seeded for 4 h, fixed, and stained with phalloidin, DAPI, and YAP1 antibody, as detailed above (Figure 4A). Outlines of the cells and their nuclei were created by hand in Fiji[56] for increased accuracy compared to cellpose software. The signal of the cytosol was calculated by subtracting the nuclear signal of each cell from the total, and the ratio for each cell (Figure 4C) was calculated according to:

$$\mathrm{YAP}_{\mathrm{cytosol}} = \mathrm{YAP}_{\mathrm{total}} - \mathrm{YAP}_{\mathrm{nucleus}} \tag{1}$$

$$\mathrm{YAP}_{\mathrm{ratio}} = \frac{\mathrm{YAP}_{\mathrm{nucleus}}}{\mathrm{YAP}_{\mathrm{cytosol}}} \tag{2}$$

Timelapse Measurement and Kymograph Analysis: For time-lapse measurements of the cells, SPY555-FastAct (Spirochrome AG, SC205) was used as a live cell dye to label F-actin. Coverslips coated with the substrates were glued into petri dishes with holes to allow for optimal imaging and were sterilized using the UV-light function of the cell culture hood for 30 min before cell seeding. Cells were cultured in FluoroBrite DMEM (Gibco, A1896701) with 10% FBS and 1% P/S. The day before the experiments, cells were incubated overnight using the FluoroBrite media with an addition of FastAct (1000× stock solution following the manufacturer's instructions) diluted 1 to 3000 to pre-label the cells. The next day cells were detached as detailed before using Trypsin and counted. 100k cells were seeded in each petri dish in the FluoroBrite media with a dilution of 1 to 2000 FastAct and five different positions per sample were selected. After about 30 min of initial attachment, the focus was adjusted and the PFS function of the microscope was activated, before recording images every minute for 4 h with the 20× objective of the Nikon Ti2 Eclipse epifluorescent inverted microscope.

After imaging, cells with a suitable signal were selected, and videos were cropped to the cell size (Figure 3D). Kymographs were created using the reslice function of Fiji,[56] and the linear actin velocity was measured using the Velocity Measurement Tool (https://dev.mri.cnrs.fr/projects/imagej-macros/wiki/Velocity_Measurement_Tool). At least 40 cells and kymographs were measured in this way for each sample (Figure 3E).

Focal Adhesion Analysis: Vinculin images were opened in Fiji,[56] cropped to only contain single cells, and a background subtraction with a rolling ball radius of ten pixels was done. Then, the auto threshold function was used to create masks of the focal adhesions followed by the analyze particles function to quantify their size and shape. A minimum size of 0.5 μm^2 was set to exclude smaller particles or artifacts from the analysis. Focal adhesion size and number were then analyzed for each cell, and the percentages of adhesions in different size ranges were calculated. Vinculin images after background subtraction can be seen in Figure 4A and the resulting data in Figure 4B and Figure S8 (Supporting Information).

Beta1 Integrin and Fibronectin Correlation Analysis: Images were opened in Fiji[56] and changed to eight-bit and 1024 × 1024 pixels for faster computation times. The actin channel was used to create outlines of the single cells, and the FN and β1 integrin channels were opened separately. The background of both was subtracted in Fiji using a rolling ball radius of 20. The two channels and respective ROIs were selected in the Coloc2 plugin of Fiji,[56] and the analysis was performed to calculate the Pearson correlation coefficient R of the FN and β1 integrin signal, with Costes significance test performed through ten iterations. An R value of 1 corresponds to perfect colocalization, 0 to no colocalization, and -1 to perfectly inverse colocalization. The results are shown in Figure 4E for the different substrates, and at least 35 different cells were analyzed for each sample.

Traction Force Measurement: Fluorescent nanoparticles were covalently bound to the surfaces of coverslips coated with the different substrates. To do this, the substrates were first silanized for 5 min through the addition of 1 mL of 3-aminopropyl trimethoxysilane (10% v/v) in ethanol. After this, the surfaces were washed with ethanol, followed by two washes with milli-Q water. FluoSpheres Carboxylate-Modified Microspheres (Invitrogen, F8807, Dark Red) with a diameter of 0.2 µm were functionalized using 1-ethyl-3-(3-dimethylaminopropyl) carbodiimide hydrochloride (EDC, Thermo Fisher Scientific, 22980) diluted to a concentration of 0.1 mg ml^{-1} in milli-Q. Nanoparticles were added to the EDC solution and were thoroughly vortexed before being added to the silanized surfaces for 1 h at room temperature. The coverslips were then washed three times using PBS, functionalized with 3.34 µg ml^{-1} as described earlier, and glued into the wells of a six-well plate with holes to improve the quality of the fluorescent images. Images of the covalently bound nanoparticles and cells growing on top can be seen in Figure S10 (Supporting Information).

The prepared wells of the plate were then filled with the FluoroBrite media containing 10% FBS and placed in the heated stage of the Nikon Ti2 epifluorescent microscope at 37 °C and 5% CO_2 for 1 h to heat up. 20 different positions were selected per sample, and the focus was set on the layer of nanoparticles. Before the cells were seeded, images of the bead layer in the selected positions were taken to be used as the undisturbed reference images in the analysis. Once images were taken, approximately 40k cells were added to each well, taking great care not to touch the plate or relevant parts of the microscope stage so as not to change the selected positions. Cells were left to spread on the substrates for 3.5 h. At this point, 50 µl of wheat germ agglutinin (WGA) Alexa Fluor 488 conjugate (Thermo Fisher Scientific, W11261) diluted in FluoroBrite was added to the cells for a final concentration of 2.5 µg ml^{-1} to allow imaging of the cell membrane. After a total of 4 h of attachment, final images of the bead layers and the cell membrane were taken.

To analyze the cellular traction generation, the average bead displacement under the cell spreading area was calculated for at least 41 cells per sample. First, the membrane staining was used to generate cell masks. Then, the images of the fluorescent nanoparticles were opened as a stack in Fiji[56], and the StackReg plugin[57] was used to align the bead layers in case of shifts in x-y-direction during the measurement. The Particle Image Velocimetry (PIV) plugin of Q. Tseng (available at https://sites.google.com/site/qingzongtseng/imagejplugins) was used to generate the displacement maps, and the cell outlines based on the membrane staining were then used to measure the average displacement for each cell in a similar fashion as described elsewhere.[58]

Statistics and Data Analysis: All the data in the graphs and text were presented as the mean ± standard deviation of the respective experiments unless stated otherwise. Statistical testing was done using GraphPad Prism (version 9.0.1), where ordinary one-way ANOVA tests with post hoc Tukey were performed. The sample size is given for each experiment in the caption of the respective figure. Statistical significance was indicated according to the following notation: *: $p < 0.05$, **: $p < 0.01$, ***: $p < 0.001$, ****: $p < 0.0001$.

Supporting Information

Supporting Information is available from the Wiley Online Library or from the author.

Acknowledgements

The authors thank all the members of the Cavalcanti-Adam laboratory for the discussion and support. This work was funded by the Deutsche Forschungsgemeinschaft (DFG, German Research Foundation) SFB 1638 Project number 511488495 and through the project "Function by Design: Cellular Hybrids" in frame of the funding initiative "Exzellenzverbünde und Universitätskooperationen" by the High Tech Agenda Bayern. The support of the Max Planck Society is also greatly acknowledged. Cartoons in **Figure 6** were created with BioRender.com.

Open access funding enabled and organized by Projekt DEAL.

Conflict of Interest

The authors declare no conflict of interests.

Data Availability Statement

The data that support the findings of this study are available from the corresponding author upon reasonable request.

Keywords

cell adhesion, elastomer, extracellular matrix assembly, substrate stress relaxation, viscoelasticity

Received: April 14, 2025
Revised: July 30, 2025
Published online:

[1] J. D. Humphrey, E. R. Dufresne, M. A. Schwartz, *Nat. Rev. Mol. Cell Biol.* **2014**, *15*, 802.
[2] E. Hadjipanayi, V. Mudera, R. A. Brown, *J. Tissue Eng. Regener. Med.* **2009**, *3*, 77.
[3] C.-M. Lo, H.-B. Wang, M. Dembo, Y. li Wang, *Biophys. J.* **2000**, *79*, 144.
[4] A. J. Engler, S. Sen, H. L. Sweeney, D. E. Discher, *Cell* **2006**, *126*, 677.
[5] O. Chaudhuri, L. Gu, M. Darnell, D. Klumpers, S. A. Bencherif, J. C. Weaver, N. Huebsch, D. J. Mooney, *Nat. Commun.* **2015**, *6*, 6364.
[6] A. Bauer, L. Gu, B. Kwee, W. A. Li, M. Dellacherie, A. D. Celiz, D. J. Mooney, *Acta Biomater.* **2017**, *62*, 82.
[7] K. Adebowale, Z. Gong, J. C. Hou, K. M. Wisdom, D. Garbett, H.-P. Lee, S. Nam, T. Meyer, D. J. Odde, V. B. Shenoy, O. Chaudhuri, *Nat. Mater.* **2021**, *20*, 1290.
[8] O. Chaudhuri, L. Gu, D. Klumpers, M. Darnell, S. A. Bencherif, J. C. Weaver, N. Huebsch, H.-p. Lee, E. Lippens, G. N. Duda, D. J. Mooney, *Nat. Mater.* **2016**, 326.
[9] W. Fan, K. Adebowale, L. Váncza, Y. Li, M. F. Rabbi, K. Kunimoto, D. Chen, G. Mozes, D. K.-C. Chiu, Y. Li, J. Tao, Y. Wei, N. Adeniji, R. L. Brunsing, R. Dhanasekaran, A. Singhi, D. Geller, S. H. Lo, L. Hodgson, E. G. Engleman, G. W. Charville, V. Charu, S. P. Monga, T. Kim, R. G. Wells, O. Chaudhuri, N. J. Török, *Nature* **2024**, *626*, 635.
[10] C. F. Guimar aes, L. Gasperini, A. P. Marques, R. L. Reis, *Nat. Rev. Mater.* **2020**, *5*, 351.
[11] O. Chaudhuri, J. Cooper-White, P. A. Janmey, D. J. Mooney, V. B. Shenoy, *Nature* **2020**, *584*, 535.
[12] O. Courbot, A. Elosegui-Artola, *NPJ Biol. Phys. Mech.* **2025**, *2*, 10.
[13] J. Weickenmeier, R. d. Rooij, S. Budday, P. Steinmann, T. Ovaert, E. Kuhl, *Acta Biomater.* **2016**, *42*, 265.
[14] R. D. González-Cruz, V. C. Fonseca, E. M. Darling, *Proc. Natl. Acad. Sci. USA* **2012**, *109*, E1523.
[15] S. R. Caliari, J. A. Burdick, *Nat. Methods* **2016**, *13*, 405.
[16] A. K. Rajendran, D. Sankar, S. Amirthalingam, H. D. Kim, J. Rangasamy, N. S. Hwang, *Biomater. Res.* **2023**, *27*, 55.
[17] R. N. Palchesko, L. Zhang, Y. Sun, A. W. Feinberg, *PLoS One* **2012**, *7*, 1.
[18] R. Xie, X. Yu, T. Cao, C. Yang, Y. Zhang, X. Wang, Y.-J. Liu, S. Duan, F. Ye, Q. Fan, *Adv. Funct. Mater.* **2023**, *33*, 2301926.
[19] N. Dwivedi, S. Das, J. Bellare, A. Majumder, *Biochem. Biophys. Res. Commun.* **2021**, *543*, 38.
[20] G. Ciccone, M. A. Gonzalez-Oliva, M. Versaevel, M. Cantini, M. Vassalli, M. Salmeron-Sanchez, S. Gabriele, *Adv. Sci.* **2025**, *n/a*, 2408635.
[21] Y. Lu, C. Chen, H. Li, P. Zhao, Y. Zhao, B. Li, W. Zhou, G. Fan, D. Guan, Y. Zheng, *Nat. Commun.* **2025**, *16*, 1365.
[22] A. Rubiano, D. Delitto, S. Han, M. Gerber, C. Galitz, J. Trevino, R. M. Thomas, S. J. Hughes, C. S. Simmons, *Acta Biomater.* **2018**, *67*, 331.
[23] C. Walker, E. Mojares, A. Del Río Hernández, *Int. J. Mol. Sci.* **2018**, *19*, 10.
[24] J. L. Voigt, J. Timmer, F. Pennarola, J. Christian, N. Meng, J. W. Blumberg, U. S. Schwarz, D. Grimm, E. A. Cavalcanti-Adam, *Advanced Functional Materials* **2024**, *34*, 2304674.
[25] E. Gutierrez, A. Groisman, *PLoS One* **2011**, *6*, 1.
[26] I. Miranda, A. Souza, P. Sousa, J. Ribeiro, E. M. S. Castanheira, R. Lima, G. Minas, *J. Funct. Biomater.* **2022**, *13*, 1.
[27] R. Moučka, M. Sedlačík, J. Osička, V. Pata, *Sci. Rep.* **2021**, *11*, 19090.
[28] E. Gutierrez, E. Tkachenko, A. Besser, P. Sundd, K. Ley, G. Danuser, M. Ginsberg, A. Groisman, *PLoS One* **2011**, *6*, e23807.
[29] C. Huerta-López, A. Clemente-Manteca, D. Velázquez-Carreras, F. M. Espinosa, J. G. Sanchez, Álvaro Martínez-del Pozo, M. García-García, S. Martín-Colomo, A. Rodríguez-Blanco, R. Esteban-González, F. M. Martín-Zamora, L. I. Gutierrez-Rus, R. Garcia, P. Roca-Cusachs, A. Elosegui-Artola, M. A. del Pozo, E. Herrero-Galán, P. Sáez, G. R. Plaza, J. Alegre-Cebollada, *Science Advances* **2024**, *10*, 46.
[30] S. Dupont, L. Morsut, M. Aragona, E. Enzo, S. Giulitti, M. Cordenonsi, F. Zanconato, J. Le Digabel, M. Forcato, S. Bicciato, N. Elvassore, S. Piccolo, *Nature* **2011**, *474*, 179.
[31] G. Nardone, J. Oliver-De La Cruz, J. Vrbsky, C. Martini, J. Pribyl, P. Skládal, M. Pešl, G. Caluori, S. Pagliari, F. Martino, Z. Maceckova, M. Hajduch, A. Sanz-Garcia, N. M. Pugno, G. B. Stokin, G. Forte, *Nat. Commun.* **2017**, *8*, 15321.
[32] A. Naba, *Nat. Rev. Mol. Cell. Biol.* **2024**, *25*, 11.
[33] A. M. Vela-Alcántara, J. Santiago-García, M. Barragán-Palacios, A. León-Chacón, M. Domínguez-Pantoja, I. Barceinas-Dávila, E. Juárez-Aguilar, E. Tamariz, *Front. Cell Dev. Biol.* **2024**, *12*, 1352233.
[34] K.-Y. Law, *J. Phys. Chem. Lett.* **2014**, *5*, 686.
[35] S. L. Voytik-Harbin, A. O. Brightman, B. Waisner, C. H. Lamar, S. F. Badylak, *In Vitro Cell. Dev. Biol. Anim.* **1998**, *34*, 239.
[36] F. Bonnier, M. Keating, T. Wróbel, K. Majzner, M. Baranska, A. Garcia-Munoz, A. Blanco, H. Byrne, *Toxicol. In Vitro* **2015**, *29*, 124.
[37] J. C. McDonald, D. C. Duffy, J. R. Anderson, D. T. Chiu, H. Wu, O. J. A. Schueller, G. M. Whitesides, *ELECTROPHORESIS* **2000**, *21*, 27.
[38] S. Park, K. Mondal, R. M. I. Treadway, V. Kumar, S. Ma, J. D. Holbery, M. D. Dickey, *ACS Appl. Mater. Interfaces* **2018**, *10*, 11261.
[39] T. Yeung, P. C. Georges, L. A. Flanagan, B. Marg, M. Ortiz, M. Funaki, N. Zahir, W. Ming, V. Weaver, P. A. Janmey, *Cell Motil. Cytoskeleton* **2005**, *60*, 24.
[40] S. Walcott, S. X. Sun, *Proc. Natl. Acad. Sci. U. S. A.* **2010**, *107*, 7757.
[41] M. A. G. Oliva, G. Ciccone, J. Luo, J. L. Voigt, P. Romani, O. Dobre, S. Dupont, M. Vassalli, M. Salmeron-Sanchez, *bioRxiv* **2024**.
[42] Q. Liu, Q. Luo, Y. Ju, G. Song, *Cancer Biol. Med.* **2020**, *17*, 282.
[43] M. Walker, E. W. Pringle, G. Ciccone, L. Oliver-Cervelló, M. Tassieri, D. Gourdon, M. Cantini, *Adv. Healthcare Mater.* **2023**, *13*, 2302571.
[44] M. Bachmann, S. Kukkurainen, V. P. Hytönen, B. Wehrle-Haller, *Physiol. Rev.* **2019**, *99*, 1655.
[45] B. Geiger, J. P. Spatz, A. D. Bershadsky, *Nat. Rev. Mol. Cell Biol.* **2009**, *10*, 21.
[46] C. G. Galbraith, K. M. Yamada, M. P. Sheetz, *J. Cell Biol.* **2002**, *159*, 695.
[47] Y. Mao, J. E. Schwarzbauer, *Matrix Biol.* **2005**, *24*, 389.
[48] C. A. Lemmon, C. S. Chen, L. H. Romer, *Biophys. J.* **2009**, *96*, 729.
[49] G. L. Lin, D. M. Cohen, R. A. Desai, M. T. Breckenridge, L. Gao, M. J. Humphries, C. S. Chen, *FEBS Lett.* **2013**, *587*, 763.
[50] M. L. Smith, D. Gourdon, W. C. Little, K. E. Kubow, R. A. Eguiluz, S. Luna-Morris, V. Vogel, *PLoS Biol.* **2007**, *5*, e268.
[51] U. S. Schwarz, J. R. D. Soiné, *Biochim. Biophys. Acta* **2015**, *1853*, 3095.
[52] R. W. Style, R. Boltyanskiy, G. K. German, C. Hyland, C. W. MacMinn, A. F. Mertz, L. A. Wilen, Y. Xu, E. R. Dufresne, *Soft Matter* **2014**, *10*, 4047.
[53] G. Ciccone, M. Azevedo Gonzalez Oliva, N. Antonovaite, I. Lüchtefeld, M. Salmerón-Sánchez, M. Vassalli, *J. Visualized Exp.* **2022**, *12*, 1352233.
[54] C. Stringer, T. Wang, M. Michaelos, M. Pachitariu, *Nat. Methods* **2021**, *18*, 100.
[55] M. Pachitariu, C. Stringer, *Nat. Methods* **2022**, *19*, 1634.
[56] J. Schindelin, I. Arganda-Carreras, E. Frise, V. Kaynig, M. Longair, T. Pietzsch, S. Preibisch, C. Rueden, S. Saalfeld, B. Schmid, J.-Y. Tinevez, D. J. White, V. Hartenstein, K. Eliceiri, P. Tomancak, A. Cardona, *Nat. Methods* **2012**, *9*, 676.
[57] P. Thévenaz, U. Ruttimann, M. Unser, *IEEE Trans. Image Process.* **1998**, *7*, 27.
[58] A. J. McKenzie, S. R. Hicks, K. V. Svec, H. Naughton, Z. L. Edmunds, A. K. Howe, *Sci. Rep.* **2018**, *8*, 7228.